NASA Technical Paper 1002

The NASA Ames Research Center One- and Two-Dimensional Stratospheric Models

Part I: The One-Dimensional Model

R. P. Turco and R. C. Whitten

SEPTEMBER 1977

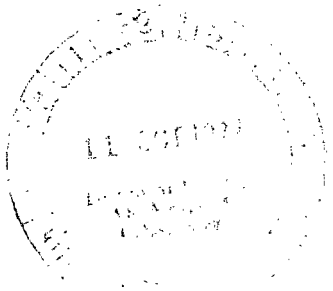

NASA

NASA Technical Paper 1002

The NASA Ames Research Center One- and Two-Dimensional Stratospheric Models

Part I: The One-Dimensional Model

R. P. Turco
R and D Associates
Marina Del Rey, California

and

R. C. Whitten
Ames Research Center
Moffett Field, California

National Aeronautics
and Space Administration

**Scientific and Technical
Information Office**

1977

THE NASA AMES RESEARCH CENTER ONE- AND TWO-DIMENSIONAL STRATOSPHERIC MODELS

PART I: THE ONE-DIMENSIONAL MODEL

R. P. Turco

R and D Associates

and

R. C. Whitten

Ames Research Center

SUMMARY

A one-dimensional model of stratospheric trace constituents, developed in a joint effort by scientists at Ames Research Center and at R and D Associates, is described in detail. Specifically, the numerical solution of the species continuity equations, including a technique for treating the "stiff" differential equations representing the chemical kinetic terms, and an appropriate method for simulating the diurnal variation of the species concentrations, are discussed. A specialized treatment of atmospheric photodissociation rates is outlined in the text. The choice of a vertical eddy diffusivity profile and its success in predicting the vertical tracer distributions (carbon 14, methane, and nitrous oxide) are also discussed.

INTRODUCTION

In this report we describe a one-dimensional atmospheric computer model. Although many of the technical details are presented here, a deeper insight into the model can be obtained from several specialized papers: the numerical integration scheme (ref. 1), the calculation of photodissociation rates (ref. 2), and the treatment of diurnal averaging (ref. 3). To be concise in this report, we emphasize the structure and philosophy of the model, and we avoid detailed tables of physical data such as photodissociation cross sections which do not affect the model performance. We also stress those characteristics of the model that differentiate it from other models. To complement this review we refer the reader to several publications that illustrate specific model simulations of: carbon compounds in the stratosphere and mesosphere (ref. 4); supersonic transport exhaust contamination at high altitudes (ref. 5); the diurnal variations of hydrogen and nitrogen compounds in the stratosphere (ref. 6); the environmental impact of hydrogen chloride released during space shuttle flights (ref. 7); the effects on ozone of nitrogen oxides generated by a nuclear war (ref. 8); fluorocarbon depletions of global ozone (ref. 9), and the formation and evolution of stratospheric aerosol particles (ref. 10).

SPECIES CONTINUITY EQUATIONS

The fundamental physical basis for all one-dimensional atmospheric models is the set of species continuity equations

$$\frac{\partial n_i}{\partial t} = P_i - n_i L_i - \frac{\partial \phi_i}{\partial z}, \qquad i = 1, 2, \ldots, I \tag{1}$$

where t is the time (sec) and z the altitude (cm), and n_i is the species concentration (cm^{-3}) (molecule units are suppressed). The terms P and L are photochemical production (cm^{-3} sec^{-1}) and loss (sec^{-1}) rates, respectively, and ϕ is the vertical particle flux (cm^{-2} sec^{-1}). According to Colegrove et al. (ref. 11), we can write the species flux (ignoring thermal diffusion) as

$$\phi_i = -\frac{K}{\gamma}\frac{\partial}{\partial z}(\gamma n_i) - D_i\left(\frac{\partial n_i}{\partial z} + \frac{n_i}{H_i} + \frac{1}{T}\frac{dT}{dz}n_i\right) \tag{2}$$

In (2), K is the eddy diffusion coefficient (cm^2 sec^{-1}), and D_i is the molecular diffusion coefficient (cm^2 sec^{-1}) for a species in air. The atmospheric scaling factor, γ, is a function of the air number density M (cm^{-3}),

$$\gamma(z) = \frac{M_o}{M(z)} \tag{3}$$

where M_o is the number density at a reference height, z_o. The scaling factor, γ, can also be related to the pressure scale height, H (cm), and air temperature, T (K), using the hydrostatic equation and the ideal gas law:

$$\gamma(z) = \frac{T_o}{T(z)} \exp\left[-\int_{z_o}^{z} \frac{dz'}{H(z')}\right] \tag{4}$$

The scale height is a function of temperature,

$$H = k_B \frac{T}{\bar{m}g} \tag{5}$$

where k_B is Boltzmann's constant (g cm^2 sec^{-2} K^{-1}), g is the gravitational acceleration (cm sec^{-2}) in the lower atmosphere, assumed to be constant with height, and $\bar{m}$ is the average mass of an air molecule (g), equivalent to about 29 amu in well-mixed air. As a check on the consistency of our adopted atmospheric structure parameters, M and T, we also calculate γ using (4) and require the results to be within about 10 percent of those from (3).

Moreover, the altitude of the change in the temperature lapse rate in the lower stratosphere is correlated with the tropopause height implied by the minimum in the eddy diffusion profile.

The species scale height, H_i (cm) in (2), like H, is defined by

$$H_i = k_B \frac{T}{m_i g} \tag{6}$$

where m_i is the species mass (g). Molecular diffusion is only important above the "turbopause" at about 100 km. In our model, we use the lower thermospheric region between 90 and 120 km as a buffer zone to insulate the numerical solutions from upper boundary effects. Accordingly, we have adopted one molecular diffusion coefficient for all of the species, and as a convenience, we define it by

$$D = v_D H \gamma \tag{7}$$

where v_D is a fixed diffusion velocity. Equation (7) implies a dependence of D on temperature and pressure, p, which is $D \propto T^2/p$; this dependence is actually very close to reality (ref. 11). We have normalized D to a value of 1.5×10^7 (cm^2 sec^{-1}) at 120 km, a typical value for atomic oxygen at this height (e.g., see ref. 11). Molecular diffusion is completely negligible in the stratosphere — indeed, most stratospheric models ignore it altogether.

When we first began solving atmospheric continuity equations we found that by scaling the species concentrations into mixing ratios using γ, we could effectively reduce diffusion gradients and obtain greater numerical stability and accuracy. Hence, in our analysis we use species mixing densities defined as

$$\rho_i = \gamma n_i \tag{8}$$

where γ can be normalized to any value (we set $\gamma = 1$ at our lower boundary). The species flux equations then become:

$$\phi_i = - \frac{(K + D)}{\gamma} \frac{\partial \rho_i}{\partial z} - v_D \rho_i (r_i - 1) \tag{9}$$

with

$$r_i = \frac{m_i}{\bar{m}} \tag{10}$$

Accordingly, we can recast the species continuity equation (1) into the form,

$$\frac{\partial \rho_i}{\partial t} = \gamma P_i - \rho_i L_i + \gamma \frac{\partial}{\partial z} \left[\frac{(K + D)}{\gamma} \frac{\partial \rho_i}{\partial z} + v_D \rho_i (r_i - 1) \right] \tag{11}$$

where P_i and L_i are evaluated using species concentrations, not mixing ratios.

At the outset of our stratospheric studies almost 6 years ago, we noted that the solutions of the species continuity equations using approximate, but very stable and efficient, numerical integration schemes could lead to the violation of mass conservation within groups of related species such as the nitrogen oxides (NO, NO_2, NO_3, N_2O_5, HNO_2, HNO_3). We overcame this problem by developing a general technique that accurately monitors the total concentrations of nearly conserved sets, or families, of compounds (ref. 1); actually, the concept of aeronomic families has a long history in the published literature. Our technique is based on an equivalent continuity equation for an entire family of gases which we obtain by summing the continuity equations of all the family members after each is multiplied by an appropriate factor, α_i, representing the weight of the species — or the number of odd-atoms of the type considered — within the family. Thus, summing (1) for a particular set of species we obtain:

$$\frac{\partial S_\ell}{\partial t} = P_{S\ell} - L_{S\ell} - \gamma \frac{\partial}{\partial z} \phi_\ell \; ; \qquad \ell = 1, 2, \ldots, L \tag{12}$$

where ℓ is the family index,

$$S_\ell = \sum_{\{i\}_\ell} \alpha_i \rho_i \tag{13}$$

$$P_{S\ell} - L_{S\ell} = \sum_{\{i\}_\ell} \alpha_i (\gamma P_i - \rho_i L_i) \tag{14}$$

$$\phi_\ell = \sum_{\{i\}_\ell} \alpha_i \phi_i \tag{15}$$

and $\{i\}_\ell$ indicates the subset of species in the ℓth family.

The family flux, which follows from (9), is

$$\phi_\ell = - \frac{(K + D)}{\gamma} \frac{\partial S_\ell}{\partial z} - v_D S_\ell (r_\ell - 1) \tag{16}$$

The factor r_ℓ in (16) is a weighted average value,

$$r_\ell = \sum_{\{i\}_\ell} \alpha_i \rho_i r_i \Big/ \sum_{\{i\}_\ell} \alpha_i \rho_i \tag{17}$$

which is nearly time invariant since the ratios of species concentrations within a family are nearly constant under most conditions. Obviously, the species boundary conditions, which we discuss later, are also additive for families.

What makes our family technique useful is that the net photochemistry for the family, represented by $P_{S\ell} - L_{S\ell}$ in (12), usually contains only slow processes which affect the total family abundance and precludes the rapid chemical interactions that occur between the family members. Accordingly, the summed continuity equations in (12) are inherently more stable than the individual species continuity equations, and their solution can be made very accurate. Another useful aspect of (12) is that these equations have the same form as (11) and, as we will see later, they can be solved with the same numerical algorithm.

Family concentrations obtained from (12) are used to correct the species abundances computed using (11). The families of species that we have utilized in our model are given in table 1 in the hierarchical order that they are

TABLE 1.- FAMILIES OF SPECIES

Hydrogen:	H(1),[a] OH(1), HO_2(1), H_2O_2(2), HNO_2(1), HNO_3(1)
Carbon:	CH(1), CH_2(1), CH_3(1), CHO(1), CH_2O(1), CH_3O(1), CH_3O_2(1), CH_4O_2(1)
Nitrogen:	N(1), NO(1), NO_2(1), NO_3(1), HNO_2(1), HNO_3(1), N_2O_5(2), $ClONO_2$(1)[b]
Sulfur:	S(1), SO(1), SO_2(1), SO_3(1), HSO_3(1), H_2SO_4(1)
Chlorine-oxide:	Cl(1), ClO(1), ClO_2(1), $ClONO_2$(1)
Odd-chlorine:	Cl(1), ClO(1), ClO_2(1), $ClONO_2$(1), HCl(1)
Bromine:	Br(1), BrO(1), HBr(1)
Oxygen:	O(1), O_3(1), O^1D(1), NO_2(1), NO_3(2), HNO_3(1), N_2O_5(3), ClO(1), ClO_2(2), $ClONO_2$(2), BrO(1)

[a] The number in parentheses is the species weight within the family.

[b] Chlorine nitrate is not corrected in the nitrogen family, but rather in the chlorine-oxide family.

solved and applied to correct the species concentrations. For example, HNO_3 is a member of the hydrogen and nitrogen families, but it is adjusted during the hydrogen correction cycle and remains fixed during the nitrogen cycle. Two types of families are easily recognizable: one in which the family

members recombine in pairs (hydrogen, nitrogen, oxygen), the other in which the members recombine with species outside of the family, or do not recombine at all (the other families). Families can also be classified according to their internal chemistry: the members of some families cycle rapidly among themselves in reaction loops (hydrogen, nitrogen, oxygen, chlorine), while the members of other families react in a chain, one species leading to the next, from the family source to its sink (carbon, sulfur). It is noteworthy that the consideration of families forces one to identify the atom carriers in aeronomic processes. For example, in the oxygen family we can readily find reactions that might not seem to involve oxygen atom transfer or recombination, but actually do; thus, the reaction of ClO with NO to form Cl and NO_2 does not involve any odd-oxygen production or loss according to our criteria for odd-oxygen (see table 1).

The family photochemical terms in (14) can be written in two ways, depending on the type of family being considered:

$$P_{S\ell} - S_\ell^2 \tilde{L}_{S\ell} \tag{18}$$

for families whose members recombine in pairs, and

$$P_{S\ell} - S_\ell \tilde{L}_{S\ell} \tag{19}$$

for the other families. These relations are logical extensions of the fact that the concentrations of family members are usually fixed fractions of the total family concentration, at least for short time periods.

There are two simple ways of correcting species concentrations using the family concentration. In the first, only the most abundant member of the family is adjusted to bring into agreement the quantities

$$S_\ell \leftrightarrow \sum_{\{i\}_\ell} \alpha_i n_i \tag{20}$$

In the second method, all of the family members are scaled by the ratio

$$S_\ell \Big/ \sum_{\{i\}_\ell} \alpha_i n_i \tag{21}$$

In the following section we discuss our application of the family correction scheme to our finite difference solutions for the species concentrations.

THE NUMERICAL SOLUTION OF THE SPECIES CONTINUITY EQUATIONS

Before presenting our detailed finite difference analysis of the species continuity equations, it is appropriate to describe the basic mechanics of our

computer model. The model extends from 10 to 120 km over a 56-point altitude grid with a 2-km vertical spacing. We presently compute the concentrations of 47 species using 123 reactions and 31 photoprocesses. Not all of the species are currently "active" ones in that their concentrations have been effectively set to zero for calculations (e.g., ammonia and the bromine compounds). Data that we initialize in the model are the atmospheric number density and temperature, vertical eddy diffusion coefficient, and species concentrations. The code internally calculates chemical rate constants and photodissociation rates using tabulated photochemical data (e.g., reaction rate activation energies and molecular absorption cross sections).

The time step control is managed as follows: for nondiurnal calculations, the initial time step τ (which is usually the minimum time step allowed) is 10^3 sec. After each computation cycle, the maximum fractional change in any of several critical species (O, O_3, NO, NO_2, H, OH, HO_2, CH_3O_2, CH_4O_2, SO_2, ClO, HCl, BrO) at any height is compared to a preset limiting value ε (usually 0.1), and if the change is more than ε, τ is halved; if the change is more than twice ε, the computation cycle is repeated until either the fractional change is less than 2ε or the minimum time step is reached. When the fractional change is less than $\varepsilon/2$, τ is increased by 25 percent. Once τ exceeds 10^5 sec, it is increased by 25 percent only when the fractional change per step is less than $(\varepsilon/2)(10^5/\tau)$, up to a maximum time step of 10^6 sec. For diurnal cycle calculations the time steps are fixed in a temporal grid over the day with the number of steps specified as an input (usually 100 steps.). The diurnal time increments are calculated by dividing 24 hr into the required number of steps using a weighting function

$$f(\chi) = \left[0.08 + 0.92(|\cos \chi|)^{1/2}\right]^{-1} \tag{22}$$

where χ is the solar zenith angle corresponding to a given time of the day.

We write the continuity equations (11) in the finite difference form:

$$\frac{\rho_{ik}^{j+1} - \rho_{ik}^{j}}{\tau} = \bar{P}_{ik}^{j} - \rho_{ik}^{j+1} L_{ik}^{j} + \frac{\gamma_k}{h}\left[\left(\frac{K_{k+\frac{1}{2}} + D_{k+\frac{1}{2}}}{\gamma_{k+\frac{1}{2}}}\right)\left(\frac{\rho_{i,k+1}^{j+1} - \rho_{ik}^{j+1}}{h}\right)\right.$$

$$+ v_D(r_i - 1)\left(\frac{\rho_{i,k+1}^{j+1} + \rho_{ik}^{j+1}}{2}\right) - \left(\frac{K_{k-\frac{1}{2}} + D_{k-\frac{1}{2}}}{\gamma_{k-\frac{1}{2}}}\right)\left(\frac{\rho_{ik}^{j+1} - \rho_{i,k-1}^{j+1}}{h}\right)$$

$$\left. - v_D(r_i - 1)\left(\frac{\rho_{ik}^{j+1} + \rho_{i,k-1}^{j+1}}{2}\right)\right], \qquad i = 1, 2, \ldots, I \tag{23}$$

where subscript i is the species index, k is the altitude level, and superscript j is the discrete time index. In our notation, quantities that are evaluated at the beginning of a time step, j, are "explicit" and are known, while quantities which are evaluated at the end of the step, that is,

at $j + 1$, are "implicit" and are to be determined during the course of the solution. The altitude increment is $h(2\times10^5$ cm), and $\bar{P}$ replaces γP in (11). The diffusive flux divergence is calculated using fluxes centered halfway between altitude levels; this assures exact mass conservation for vertical diffusion. The terms K, D, and γ are computed at the midlevel points, $k + \frac{1}{2}$, using a logarithmic interpolation, or equivalently, as

$$K_{k+\frac{1}{2}} = (K_k K_{k+1})^{\frac{1}{2}} \tag{24}$$

for example.

Equation (23) can be put in the convenient form,

$$\rho^{j+1}_{i,k+1} A_{ik} + \rho^{j+1}_{ik} B^j_{ik} + \rho^{j+1}_{i,k-1} C_{ik} = E^j_{ik} \quad , \qquad i = 1, 2, \ldots, I \tag{25}$$

with

$$\left.\begin{aligned}
A_{ik} &= -\frac{\gamma_k}{h^2}\left(\frac{K_{k+\frac{1}{2}} + D_{k+\frac{1}{2}}}{\gamma_{k+\frac{1}{2}}}\right) - \frac{\gamma_k v_D}{2h}\,(r_i - 1) \\
B^j_{ik} &= \frac{1}{\tau} + L^j_{ik} + \frac{\gamma_k}{h^2}\left(\frac{K_{k+\frac{1}{2}} + D_{k+\frac{1}{2}}}{\gamma_{k+\frac{1}{2}}} + \frac{K_{k-\frac{1}{2}} + D_{k-\frac{1}{2}}}{\gamma_{k-\frac{1}{2}}}\right) \\
C_{ik} &= -\frac{\gamma_k}{h^2}\left(\frac{K_{k-\frac{1}{2}} + D_{k-\frac{1}{2}}}{\gamma_{k-\frac{1}{2}}}\right) + \frac{\gamma_k v_D}{2h}\,(r_i - 1) \\
E^j_{ik} &= \frac{\rho^j_{ik}}{\tau} + \bar{P}^j_{ik}
\end{aligned}\right\} \tag{26}$$

The solution matrix for the ρ^{j+1}_i in (25) is tridiagonal, and there is a simple and fast technique for its inversion (e.g., ref. 12). The method is based on a coupling equation between the solution values at adjacent altitude levels,

$$\rho^{j+1}_{ik} = U^j_{ik} - V^j_{ik}\rho^{j+1}_{i,k+1} \tag{27}$$

Substitution of (27) into (25) leads to the recurrence relationships for U and V:

$$\left.\begin{aligned}
U^j_{ik} &= \left(E^j_{ik} - U^j_{i,k-1} C_{ik}\right) \Big/ \left(B^j_{ik} - V^j_{i,k-1} C_{ik}\right) \\
V^j_{ik} &= -A_{ik} \Big/ \left(B^j_{ik} - V^j_{i,k-1} C_{ik}\right)
\end{aligned}\right\} \tag{28}$$

To proceed with our finite difference solution, we must first discuss the species boundary conditions in our model.

For each species, we specify a lower boundary flux ϕ_{io} and an upper boundary flux, ϕ_{iu}, which may be fixed or have a specified time dependence. But at the lower boundary we also include a flux component,

$$\phi_{Bi} = v_{Bi}(n_{Bi} - \rho_{i1}) \tag{29}$$

by defining the "velocity" at the boundary, v_{Bi}, and concentration, n_{Bi} (if n_{Bi} is zero, our code sets $\phi_{Bi} = 0$ automatically). Whenever we use boundary condition (29), we usually set the boundary velocity, v_B, to 1 cm sec^{-1}, which is a typical value for the troposphere. The flux condition (29) is equivalent to a solution of the steady-state species continuity equation between the ground and the lower boundary at 10 km using known surface boundary conditions and tropospheric process rates for a particular constituent. In other words, equation (29) establishes a loose connection between tropospheric processes and the species boundary conditions at 10 km. Hence, boundary condition (29) can be used to summarize, in a simplified way, the effects on species concentrations of the chemistry and motions in the lower atmosphere. Considering the crudeness of our knowledge about tropospheric aeronomy, a very simple treatment of tropospheric processes in this manner is certainly appropriate.

The use of boundary condition (29) for long-lived, well-mixed gases like CO_2, N_2O, and CH_4 is straightforward — we set n_{Bi} to the concentrations we wish them to attain, and they are adjusted automatically. The ambient troposphere is normally an efficient sink for many gases (e.g., the nitrogen oxides, HCl). In these cases, we usually set n_B to a small concentration, often to 1, unless observations in the upper troposphere are available. We treat the nitrogen oxides somewhat differently, however. First, we specify their total lower boundary concentration, $S_B(NO_x)$, which we use to calculate their total boundary flux; then we apportion this flux among the individual species according to their instantaneous abundances. For chemically active radicals (e.g., O, OH, Cl) we simply set $\phi_O = \phi_u = 0$, and also, $n_B = 0$. In the past we have only exploited the more general application of boundary condition (29) during specific pollution studies involving fluorocarbons and HCl.

In our model, when we utilize an eddy diffusion profile with a sharp, very stable tropopause level, usually located between 13 and 16 km, the boundary conditions at 10 km have little effect on our solutions (except for the uniformly mixed constituents, of course). In this situation, the transport barrier at the tropopause effectively decouples the troposphere and the stratosphere for many of the air constituents.

The boundary conditions that are currently used in our model are summarized in table 2. During computer runs, we print out the boundary specifications and the boundary fluxes for each species and use them to check the accuracy and convergence of our solutions. For example, we can balance the hydrogen atom flow via H_2, H_2O, and CH_4 at 10 km, and we can

TABLE 2.- SPECIES BOUNDARY CONDITIONS[a]

Species[b,c]	Lower boundary concentration at 10 km, cm^{-3}	Fixed upper boundary flux at 120 km, cm^{-2} sec^{-1}
O	0	-1.0(11)
O_3	3.0(11)[d]	0
NO	*e*	-2.0(8)
NO_2	*e*	0
HNO_2	*e*	0
HNO_3	*e*	0
N_2O	2.6(12)	0
N_2O_5	*e*	0
H	0	1.0(7)
H_2	4.0(12)	0
H_2O	3.0(13)	0
CH_4	1.0(13)	0
CO	3.0(11)	0
CO_2	3.0(15)	0
HCl	1.0(6)	0
CF_2Cl_2	1.6(9)	0
$CFCl_3$	9.0(8)	0
CCl_4	1.0(9)	0
CH_3Cl	5.0(9)	0

[a] All species have zero fixed lower boundary fluxes.

[b] Species not listed here have zero lower boundary concentrations, n_B, and zero fixed upper fluxes, ϕ_u, except for H_2O_2, CH_4O_2, SO_2, H_2SO_4, and $ClONO_2$ which have $n_B = 1$.

[c] Inactive species not listed here are: NH_3, Br, BrO, HBr.

[d] 3.0(11) = 3.0×10^{11}.

[e] The total lower boundary concentration, n_B, for the nitrogen oxides is 1.0(6).

match the total chlorine atom efflux from the stratosphere against the integrated production rate.

With the boundary conditions so defined, we can not proceed with the development of our numerical solution. The species continuity equations at the lower boundary are written:

$$\frac{\rho_{i1}^{j+1} - \rho_{i1}^{j}}{\tau} = \bar{P}_{i1}^{j} - \rho_{i1}^{j+1} L_{i1}^{j} + \frac{1}{h}\left[\left(\frac{K_{3/2} + D_{3/2}}{\gamma_{3/2}}\right)\left(\frac{\rho_{i2}^{j+1} - \rho_{i1}^{j+1}}{h}\right)\right.$$

$$+ v_D(r_i - 1)\left(\frac{\rho_{i2}^{j+1} + \rho_{i1}^{j+1}}{2}\right) - (K_1 + D_1)\left(\frac{\rho_{i2}^{j+1} - \rho_{i1}^{j+1}}{2h}\right)$$

$$\left. - v_D(r_i - 1)\rho_{i1}^{j+1}\right] \tag{30}$$

where we recognize that the lower boundary-layer thickness is only $h/2$ cm. The flux condition at the lower boundary is expressed as

$$\phi_{io} + v_{Bi}(n_{Bi} - \rho_{i1}^{j+1}) = -(K_1 + D_1)\left(\frac{\rho_{i2}^{j+1} - \rho_{i1}^{j+1}}{2h}\right) - v_D(r_i - 1)\rho_{i1}^{j+1} \tag{31}$$

In our scheme we have allowed for an "image" concentration, ρ_{io}^{j+1}, a distance h below the lower boundary. After eliminating ρ_{io}^{j+1} from (30) and (31), the resulting expression can be rearranged to yield

$$\rho_{i1}^{j+1} = U_{i1}^{j} - V_{i1}^{j}\rho_{i2}^{j+1} \tag{32}$$

Equation (32) defines U_{i1}^{j} and V_{i1}^{j} for each species, and these quantities can be used with (26) and (28) to determine the U and V terms at every other altitude level for all the species.

We note that our formulation of the boundary equations allows the species boundary concentrations to be affected not only by local flux divergences, but by photochemistry as well. A simpler, well-known boundary specification which requires that

$$\phi(\text{boundary}) = -(K_1 + D_1)\left(\frac{\rho_{i2}^{j+1} - \rho_{i1}^{j+1}}{h}\right) - v_D(r_i - 1)\rho_{i1}^{j+1} \tag{33}$$

artificially connects the solution for ρ_{i1} and ρ_{i2} together by a mixing ratio gradient attributable only to transport.

The upper boundary condition is treated like the lower one. That is, we write a continuity equation at the upper level analogous to (30) except that we utilize an "image" density above the upper boundary, $\rho_{i,u+1}^{j+1}$ (where u is the index for the uppermost altitude interval). We also have a flux condition like (31) for the upper boundary. Moreover, we know the recurrence relationship, (27), for level $k = u - 1$ (i.e., we have previously determined the quantities $V_{i,u-1}^{j}$ and $U_{i,u-1}^{j}$). Accordingly, with these three equations

we can eliminate $\rho^{j+1}_{i,u-1}$ and $\rho^{j+1}_{i,u+1}$ and solve for ρ^{j+1}_{iu}, which turns out to be:

$$\rho^{j+1}_{iu} = \frac{E^j_{iu} - 2(\gamma_u/h)\phi_{iu} - 2C^j_{iu}U^j_{i,u-1}}{(1/\tau) + L^j_{iu} + 2(\gamma_u/h)v_D(r_i - 1) - 2C^j_{iu}\left(1 + V^j_{i,u-1}\right)} \tag{34}$$

The species concentrations below the upper boundary are obtained at the descending levels, $u - 1$, $u - 2$, . . . 1, using (27), the known U and V coefficients, and the calculated species concentration at the next highest level. Obviously, by solving the species continuity equations in sequence, $i = 1, 2, \ldots, I$, only one pair of U and V vectors are needed, and these can be recycled for each species.

The family continuity equations described by relationships (12)-(19), are solved in the same way as the species continuity equations. There are two procedural differences that must be mentioned, however. First, the family photochemical loss rate in (12) is linearized in the implicit variable $S^{j+1}_{\ell u}$, which leads to the following numerical generalization of (18) and (19):

$$\hat{P}^j_{S\ell k} - S^{j+1}_{\ell k}\hat{L}^j_{S\ell k} \tag{35}$$

The definitions of $\hat{P}_S$ and $\hat{L}_S$, which are straightforward, are given by Turco and Whitten (ref. 1). The second procedural difference is that the family boundary conditions must be established by summing (30) and (31) — and the corresponding relations at the upper boundary — for each family. During this exercise, all the terms that include a species subscript (i.e., those containing r_i, v_{Bi}, n_{Bi}, ϕ_{iO}, or ϕ_{iu}) must be redefined as average values at the beginning of the time step; for example,

$$r^j_{\ell k} = \sum_{\{i\}_\ell} \alpha_i r_i \rho^j_{ik} \Big/ \sum_{\{i\}_\ell} \alpha_i \rho^j_{ik} \tag{36}$$

The family continuity equations (12) and (16), when cast in the finite difference form of (23), and after the application of the specialized treatment of the photochemical terms and boundary conditions just described, are solved algebraically exactly like equations (23)-(34) for the individual species.

For our model, the extra computer time required to handle the families is about 10 percent of the total computer expenditure, which is more than offset by a large gain in numerical speed and stability. Another numerical note: since we determine the species concentrations first, we can then use both the ρ^j_{ik} and ρ^{j+1}_{ik}, or their average value, to compute the family chemical production and loss rates, thereby further improving the solution characteristics.

The family concentrations are used to correct the computed species concentrations in our model. In this sense, our method is more sophisticated than techniques that only compute family concentrations and then assign each member an abundance based on steady-state photochemical ratios. Our basic correction scheme, which is performed automatically in the code, is to adjust only the most abundant family member; this leads to the correction equation

$$\rho_{ik}^{j+1}(\text{corr.}) = \left(S_{\ell k}^{j+1} - \sum_{\substack{\{i'\}_\ell \\ i' \neq i}} \alpha_{i'} \rho_{i'k}^{j+1} \right) \Big/ \alpha_i \tag{37}$$

For the carbon and sulfur families, however, all of the species are adjusted using a scaling factor,

$$\rho_{ik}^{j+1}(\text{corr.}) = \rho_{ik}^{j+1} \left(S_{\ell k}^{j+1} \Big/ \sum_{\{i\}_\ell} \alpha_i \rho_{ik}^{j+1} \right) \tag{38}$$

Our correction scheme is effective for at least two reasons:

1. In most cases, numerically generated concentration imbalances among the members of a family are quickly redistributed by the fast photochemical coupling among these species.

2. During a calculation, the species concentrations are restricted to maximum changes of about 10 percent or less per step, and the family concentration variations are usually much smaller than this, so that the actual correction per step is normally a very small fraction.

We note that a species is adjusted only once in the correction hierarchy given in table 1. In some cases, at specific altitudes, the correction scheme itself may become unstable because the numerical system is overdetermined. For example, when two species in a family have almost equal concentrations, an unstable oscillation can develop where one species is corrected at one time step, the other at the next step. This problem is eliminated by explicitly stating which species is to be corrected each time. These isolated instabilities are easily handled in the computer program. In our code, we have achieved absolute solution convergence with time steps as large as 10^7 sec (i.e., about 3 steps per year), and we could easily do even better.

AERONOMICAL MODEL PARAMETERS

We will now discuss some of the aspects of the atmospheric physics and chemistry which we have included in our model.

The rate coefficients used in our calculations are temperature and pressure dependent, wherever appropriate. For the most part, we have adopted the standard rate constant values from published data lists (e.g., the National Bureau of Standards Reports — also see refs. 4 to 10 for tabulations of our rate coefficients). Whenever a new rate constant is introduced in our work or an old one is adjusted to achieve some aeronomical state, it is usually discussed in detail. For several important altitude-dependent rate coefficients, most notably those for the formation reactions of HNO_3 from OH and NO_2 and of N_2O_5 from NO_2 and NO_3, we have developed analytical pressure- and temperature-dependent expressions for the coefficients using steady-state multilevel kinetics, thereby eliminating the need for tables of data (see ref. 9).

The rate constants for the critical reactions,

$$OH + HO_2 \rightarrow H_2O + O_2 \tag{39}$$

$$O + HO_2 \rightarrow OH + O_2 \tag{40}$$

are still controversial. In our model, using values of 5.0×10^{-11} cm^3 sec^{-1} for k_{39} and 3.0×10^{-11} cm^3 sec^{-1} for k_{40} leads to a total integrated daytime OH column abundance of about 8×10^{13} cm^{-2}, close to that detected by Burnett (ref. 13). It is noteworthy, however, that the variability in Burnett's data encompasses nearly an order of magnitude about a value of 1×10^{14} cm^{-2}. Our stratospheric OH concentrations are still somewhat lower than the observations of Anderson (ref. 14) after adjusting his values upward by a factor of 2 to roughly account for the ratio of OH abundances in full daylight to those at the experimental zenith angle of 80°.

In our computer code, rate constants and the corresponding chemical production and loss terms in the species continuity equations are manipulated automatically; a five-number label for each reaction is used to specify the reactants and products. Moreover, by scanning the reaction label and comparing the species involved with templates of family constituents, the reactions affecting the families are flagged for quick future reference. As a check on the automatic chemistry routine, the atom balances for each reaction are displayed as output at the start of every computer run.

We calculate atmospheric photodissociation rates using the well-known optical depth formulations of light absorption, and the set of wavelength intervals listed in table 3. In this case,

$$J_\nu = \sum_\mu F_\mu \sigma_{\nu\mu} \exp[-\tau_\mu(z,\chi)] \tag{41}$$

where J_ν is the photorate (sec^{-1}) for process ν; μ is the wavelength interval index; F_μ is the total incident solar flux (photons cm^{-2} sec^{-1}) at the top of the atmosphere in the wavelength interval μ $\sigma_{\nu\mu}$ is the cross section (cm^2) for process ν in interval μ; and τ_μ is the corresponding optical depth at the height z and solar zenith angle χ. The optical depth is defined by

TABLE 3.- WAVELENGTH INTERVALS USED TO CALCULATE PHOTODISSOCIATION RATES

Wavelength range, nm	Number of bins in the range	Bin width, nm
121.6	1	0.1
137.5-177.5	8	5.0
177.5-177.75	1	.25
177.75-201.25[a]	47	.5
201.25-202.5	1	1.25
202.5-347.5	29	5.0
347.5-350	1	2.5
350-750	8	50

[a]In this wavelength region, each 0.5-nm bin is subdivided into five 0.1-nm intervals for O_2 Schumann-Runge band absorption data.

$$\tau_\mu(z,\chi) = C_2(z,\chi)\sigma_{2\mu} + \tau_\mu^{SR}(z,\chi) + C_3(z,\chi)\sigma_{3\mu} \tag{42}$$

where subscripts 2 and 3 refer to O_2 and O_3, respectively; C in each case is the integrated molecular column (cm^{-2}) from the point of observation (z,χ) to the sun, σ_2 and σ_3 are continuum absorption coefficients (cm^2), and τ^{SR} is the O_2 Schumann-Runge band optical depth, which we will discuss shortly. We have ignored other atmospheric absorbers of solar radiation such as NO_2 since their effects on photorates are negligible.

Our solar fluxes are taken from Ackerman (ref. 15) above 300 nm and Donnelly and Pope (ref. 16) below 300 nm; the latter fluxes, for a moderate level of solar activity, represent a compromise between Ackerman's larger values and recently observed lower values (e.g., ref. 17). In our calculations we do not account for Rayleigh multiple scattering of sunlight, but we do roughly account for the effective planetary albedo by increasing the incident flux, F, by an albedo factor, α (e.g., see ref. 18):

$$\alpha = \begin{cases} 0.40 & \lambda > 320 \text{ nm} \\ 0.40\left[\dfrac{\lambda - 300}{20}\right] & 300 \le \lambda \le 320 \text{ nm} \\ 0 & \lambda < 300 \text{ nm} \end{cases} \tag{43}$$

so that

$$F \rightarrow F(1 + \alpha) \tag{44}$$

We calculate the integrated O_2 column density, C_2, using the optical depth factor approximation for an exponential atmosphere which is based on the Chapman function (refs. 19 and 20). For this calculation we assume that O_2 comprises 21 percent of the total number of air molecules, and we use our model temperature profile to evaluate the appropriate scale heights. We calculate the ozone column, C_3, by numerically integrating the instantaneous ozone distribution in the model along a ray from the point of observation to the sun using a logarithmic interpolation scheme (ozone concentrations below 10 km are specified as input, and those above 120 km are extrapolated exponentially assuming a 3-km scale height). Thus,

$$C_3 = \sum_k \left| s_{k+1} - s_k \right| \overline{[O_3]}_k \tag{45}$$

where s_k is a path length defined by

$$s_k = (r_k^2 - r_m^2)^{1/2} \tag{46}$$

with r_k being the distance (cm) from the Earth's center to the altitude level k, and r_m the perpendicular distance (cm) to the (extended) ray of observation, and where

$$\overline{[O_3]}_k = ([O_3]_{k+1} - [O_3]_k)/\ln([O_3]_{k+1}/[O_3]_k) \tag{47}$$

with the brackets ([ ]) indicating a concentration.

Before Hudson and Mahle (ref. 21) had published their parameterized equations for calculating O_2 Schumann-Runge band absorption, we had already treated this absorption in detail using a band model. Blake et al. (ref. 22), who collected O_2 absorption data in the S-R band region with an instrument having about a 0.1-nm resolution, showed that the observed O_2 S-R band optical depth depended simply on the square root of the O_2 column density for a wide range of optical depths. This square root absorption law has been used by Brinkmann (ref. 23) to study water vapor dissociation in the terrestrial atmosphere. In our model, we define the O_2 optical depth in the Schumann-Runge bands as

$$\tau_{SR} = \begin{cases} \sigma_{SR} C_2 / \tau_w^{SR} & \tau^{SR} < \tau_w^{SR} \\ (\sigma_{SR} C_2)^{1/2} & \tau_w^{SR} \le \tau^{SR} \le \tau_s^{SR} \\ \sigma_{SR} C_2 / \tau_s^{SR} & \tau_s^{SR} < \tau^{SR} \end{cases} \tag{48}$$

Here σ_{SR} is the O_2 absorption cross section obtained from Blake et al. (ref. 22) at 0.1-nm intervals in the S-R band system (177.75-201.25 nm). In analyzing the Blake et al. data, we have accounted for O_2 continuum

absorption and its apparent increase at high experimental absorption cell pressures (see ref. 2). The parameters τ_w^{SR} and τ_s^{SR} are the weak and strong absorption limits beyond which the simple square root absorption law is inapplicable. In the weak absorption limit, we choose $\tau_w = 0.15$ to obtain the correct integrated oscillator strength for the bands. Blake et al. (ref. 22) found that their absorption cross sections displayed a square root dependence on the O_2 column density up to $\tau^{SR} \sim 3$. In numerical experiments, we have found that none of our photorates are influenced by more than 5 percent for any selection of $\tau_s^{SR} \geq 2$; accordingly, we let $\tau_s^{SR} \to \infty$ in our model.

Using a band absorption model, the O_2 photodissociation rate in the S-R bands is easily calculated since it is simply proportional to the derivative with respect to C_2 of the corresponding optical transmission factor. In (41), this is equivalent to substituting for $\sigma_{\nu\mu}$,

$$\sigma^{SR} = \Omega\tau^{SR} \Big/ C_2 \tag{49}$$

where

$$\Omega = \begin{cases} 1, & \tau^{SR} < \tau_w^{SR}, \quad \text{or} \quad \tau^{SR} > \tau_s^{SR} \\ \frac{1}{2}, & \tau_w^{SR} \leq \tau^{SR} \leq \tau_s^{SR} \end{cases} \tag{50}$$

Except for the O_2 S-R band data, the absorption cross sections for other species are specified every 0.5 nm in the S-R band region (although they probably only need to be specified every 2.0-5.0 nm). In each of these 0.5-nm wavelength bins, we calculate an average O_2 S-R band transmission factor and dissociation cross section:

$$\left\langle e^{-\tau^{SR}} \right\rangle = \frac{1}{5} \sum_{\xi=1}^{5} e^{-\tau_\xi^{SR}} \tag{51}$$

$$\left\langle \sigma^{SR} e^{-\tau^{SR}} \right\rangle = \frac{1}{5} \sum_{\xi=1}^{5} \sigma_\xi^{SR} e^{-\tau_\xi^{SR}} \tag{52}$$

where the index ξ ranges over the five 0.1-nm bins within the 0.5-nm interval. The quantities defined by (51) and (52) are inserted directly into (41).

We have made detailed comparisons (refs. 2 and 24) between the O_2 absorption and dissociation profiles calculated with our band model and those from the Hudson and Mahle model (ref. 21); the agreement is better than about 10 percent in the stratosphere and about 25 percent in the mesosphere. This correspondence is excellent, considering that the two results are derived from completely independent data bases, and that no tuning of the band model (to account for temperature effects and instrumental uncertainties on the observed low-resolution absorption cross sections) has been performed. The

band absorption model also preserves the simple optical depth formalism and is therefore easy to include in existing photodissociation rate algorithms.

Our species photodissociation cross sections are given in reference 2. Newer data, not listed in reference 2, are used for the $O(^1D)$ quantum yield from O_3 photolysis (refs. 25 and 26) and for the absorption cross sections of N_2O (ref. 27), HCl (ref. 28), ClO (private communication from Jaffe, Ames Research Center, 1976), and $ClONO_2$ (ref. 29).

In our model we can select one of several options for computing photorates. For diurnal calculations, the rates are calculated at a fixed set of zenith angles corresponding to the fixed diurnal time grid mentioned earlier (the latitude and season which are selected also determine the zenith angles). For nondiurnal runs, we can compute photorates at a fixed zenith angle specified by a latitude, earth declination, and time of day. Or, we can compute, in two different ways, photodissociation rates which are averaged over a 24-hr day: 1) by determining the rates at up to 50 zenith angles over one-half the day and numerically averaging these values; and 2) by estimating the rates using an approximation described by Rundel[1] for spring/fall conditions:

$$\bar{J} \approx \frac{c_O}{1 + b_O \tau^{n_O}} J(\chi_{noon}) \tag{53}$$

with $c_O = 0.5$, $b_O = 0.835$, $n_O = 0.619$, and $\chi_{noon} = 30°$. We have found that Rundel's approximation gives results in good accord with the diurnally time-averaged rates.

Cogley and Borucki (ref. 30) have calculated average photodissociation rates using the approximation

$$\bar{J} = \tilde{c}_O J(\tilde{\chi}_O) \tag{54}$$

We have compared photorates computed using (53) with those from (54) when $\tilde{c}_O = 0.5$ and $\tilde{\chi}_O = 55°$. For the most part, the values are within 5-10 percent of each other. However, in regions of strong absorption the differences become quite large, and in this case, Rundel's predictions are generally more satisfactory. Still, it is not clear whether, in the O_2 Schumann-Runge band absorption region, more than one set of parameter values is needed for the Rundel model because of the complex dependence of the S-R optical depth on the molecular oxygen column density.

Modeling techniques that only use averaged photodissociation coefficients to simulate diurnal effects can often give incorrect and misleading results

[1]Private communication from R. D. Rundel, Johnson Space Flight Center, 1976.

for the abundances of many stratospheric gas constituents and for the net depletion of ozone by chlorine oxides. Therefore, we have developed a simple scheme for modifying the species continuity equations that accurately accounts for the effects of diurnal variations on computed species concentrations and ozone perturbations (ref. 3). To do this, we average the continuity equations over a 24-hr day and derive equivalent relations for the average concentrations $\bar{n}_i$:

$$\frac{\partial \bar{n}_i}{\partial t} = \sum_{j,k} \varepsilon_{ijk} \beta_{jk} k_{jk} \bar{n}_j \bar{n}_k - \frac{\partial}{\partial z} \phi(\bar{n}_i) \tag{55}$$

Here, k_{jk} is a generalized rate constant which can be a photodissociation rate; ε_{ijk} is ± 1 depending on whether the species i is produced or destroyed, respectively, by reaction (jk); and $\phi(\bar{n}_i)$ is the average species flux evaluated using the height distribution $\bar{n}_i$. In our approximation, the average species concentration $\bar{n}_i$ is divided into two components, the average daytime and nighttime species abundances n_i^D and n_i^N, respectively, so that:

$$\bar{n}_i = n_i^D \frac{T_D}{T} + n_i^N \frac{T_N}{T} \tag{56}$$

where T_D and T_N are the daytime and nighttime durations, respectively, and T is the sum of T_D and T_N. During a given diurnal cycle, a species' daytime and nighttime concentrations are assumed to be constant at their respective average values, n^D and n^N; hence, our solution scheme parameterizes diurnal variations in the form of a simple, two-level step function. With this assumption, it is then convenient to define the quantities

$$\alpha \equiv \frac{\bar{n}_i}{n_i^D} = \frac{T_D}{T} + r_i \frac{T_N}{T} \tag{57}$$

where r_i is the nighttime-to-daytime species concentration ratio

$$r_i = n_i^N \Big/ n_i^D \tag{58}$$

In terms of the parameters r_i and α_i, the rate constant scaling factor β_{jk} in (57) is

$$\beta_{jk} = \left(\frac{T_D}{T} + \frac{T_N}{T} r_j r_k \right) \Big/ \alpha_j \alpha_k = 1 + \frac{T_D}{T_N} \left(1 - \alpha_j^{-1}\right)\left(1 - \alpha_k^{-1}\right) \tag{59}$$

The β factor is obviously 1 unless *both* of the reactants have diurnal variations. In (55) the photodissociation processes take the form

$$\bar{J}_i \bar{n}_i \Big/ \alpha_i \tag{60}$$

where $\bar{J}$ is a 24-hr averaged photorate that can be computed using any one of the several techniques discussed earlier.

Our diurnal averaging scheme quantifies the effects of nighttime chemistry on the average day-to-day abundances of air constituents by adjusting the appropriate photochemical rate constants to account for the presence at night of certain reactant gases. Our step function approximation for diurnal variations greatly simplifies the evaluation of the 24-hr average rates of the nonlinear photochemical interaction terms in the species continuity equations. The relative magnitudes of the two-level diurnal species abundances are parameterized using the night-to-day concentration ratios, r_i. For most stratospheric constituents, these concentration ratios are either effectively 0 or 1. For other species we can calculate r values by using simplified nighttime chemical reaction schemes, assuming as initial sunset conditions the appropriate daytime species concentrations and ignoring the effects of transport on the ratios. This approach leads to r values that are functions of the model (rate constants and species concentrations), and can be updated accordingly during computer simulations. Actually, the concentration ratios are nearly invariant quantities that could, for example, be calculated using the results of a diurnally varying model simulation.

The averaged species continuity equations in (55) have exactly the same form as (1) and can therefore be solved in the manner we have already described. In fact, in our model we can turn our averaging procedure on or off quite simply. Furthermore, since the form of the family continuity equations is also unaffected by our averaging technique, their solution also proceeds just as before. Once the average species concentrations, $\bar{n}_i$, are calculated, we can obtain daytime and nighttime abundances using (57) and (58).

We have compared the predictions of our averaged model with those of a diurnally varying model (ref. 3); typically, the calculated concentrations are within 10 percent of each other, but with larger differences of up to 20 percent occurring at some altitudes (usually where a species is decreasing rapidly and has a very small absolute abundance). This is in striking contrast to the large errors obtained from a model using only averaged photodissociation rates where, for example, an order of magnitude underestimate of the N_2O_5 concentration results.

Our model calculates the light emission intensities of vibrationally excited $OH^{\ddagger}$ and electronically excited $O_2(^1\Delta_g, {}^1\Sigma_g^+)$ molecules in the atmosphere. Predicted column-integrated emission rates have been compared with observations to provide a constraint on the model parameters. For $OH^{\ddagger}$, photon efficiencies (i.e., the number of photons emitted for each $OH^{\ddagger}$ formed by reaction) in the vibrational sequences $\Delta v = 1, 2, 3$ are calculated with a detailed vibrational state model for $OH(X\ ^2\Pi, v = 1, 9)$, which includes radiation cascading and chemical and collisional quenching. For the O_2 singlet delta states, we have incorporated all of the known photochemical excitation and quenching mechanisms in our computer simulation.

We have already mentioned our eddy diffusion coefficient, K, whose values are given in figure 1. Our profile is similar in its general characteristics to one originally proposed by Wofsy and McElroy (ref. 31), but with some important differences. Our diffusivities are based in part on meteorological considerations and in part on the successful prediction of the observed distributions of several atmospheric tracers — in particular, methane, nitrous oxide, and carbon 14. The troposphere, which is usually marginally stable or unstable, is usually subjected to strong mixing motions that are characterized by a large vertical eddy diffusion coefficient ($\sim 3\times10^5$ cm^2 sec^{-1}). However, above the tropopause, where the temperature lapse rate decreases sharply, the stratospheric air mass is highly stable and very resistant to vertical displacements. Typically, vertical velocities just above the tropopause are only about 1 percent of those found in the troposphere. Hence, we expect the eddy diffusivity also to change abruptly at the tropopause, as indicated in figure 1. In our model we have fixed the tropopause height at 13 km, which is a representative value for midlatitudes. Even though the entire stratosphere is thermodynamically stable, we know, by observing the distributions of inert tracers like carbon 14 in the lower stratosphere and photochemically active species like methane at greater altitudes, that the effective vertical diffusion velocity increases with increasing height above the tropopause. This property is reflected in the shape of our eddy diffusion profile above the tropopause.

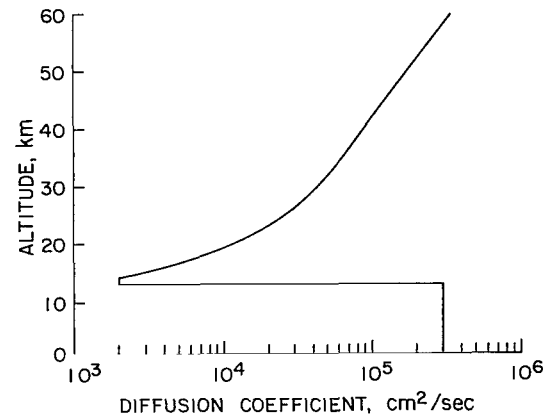

Figure 1.- The eddy diffusion coefficient (K) profile used in some of our one-dimensional model studies.

The stratospheric distributions of carbon 14 resulting from atmospheric thermonuclear explosions have been measured following the nuclear bomb tests of the early 1960s (e.g., see ref. 32). Accordingly, we have adjusted the lower portion of our eddy diffusion profile so that our model predicts C^{14} distributions which, even after 2 years of atmospheric relaxation following a nuclear detonation, are still close to the observed values. This agreement is illustrated in figure 2(a). Johnston et al. (ref. 32), in their analysis of the carbon 14 data, have concluded that it would be difficult to reproduce most of the carbon 14 observations using eddy diffusion coefficients with a tropopause level higher than 13 km, and we also find this to be true.

In the upper stratosphere, the predicted vertical distributions of selected "tracer" gases such as methane and nitrous oxide are not independent of photochemistry. Indeed, new laboratory measurements of photolysis cross sections and reaction rate constants often necessitate adjustments of the eddy diffusion profile. In addition, the selection of eddy diffusivities

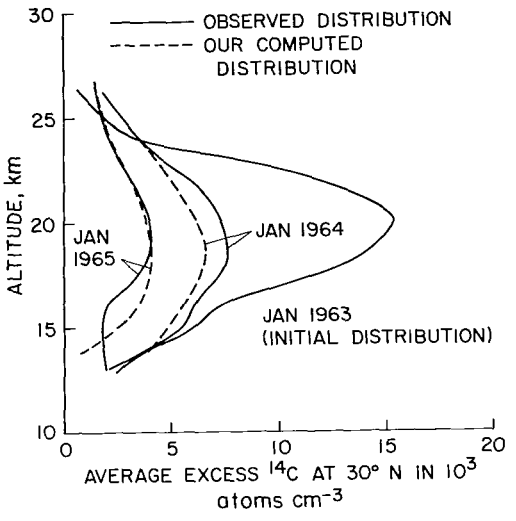

(a) Carbon 14 observations are represented by solid lines (see ref. 32), predicted distributions by broken lines.

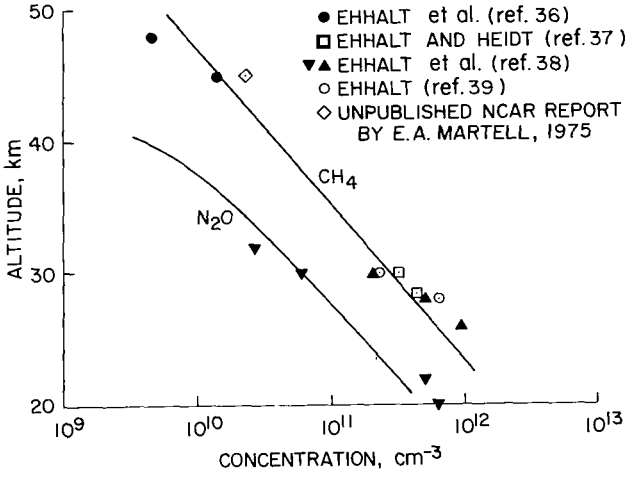

(b) Observed and predicted vertical distributions of methane and nitrous oxide.

Figure 2.- Vertical distributions of carbon 14, methane, and nitrous oxide.

at the higher altitudes also depends on the manner in which constituents with large day-to-night concentration variations are averaged over the diurnal cycle. For example, methane is decomposed principally by its reaction with OH in the stratosphere and mesosphere,

$$OH + CH_4 \rightarrow H_2O + CH_3 \qquad (61)$$

Since OH disappears rapidly after sunset, as a consequence of reaction (39), the predicted total amount of methane destroyed in a day is less for a model which diurnally averages the OH abundance than for a model which does not. In our case, using the averaging procedure outlined earlier, the upward flux of CH_4 required to maintain its high-altitude distribution is smaller than would otherwise be expected. Therefore, our diffusion coefficients have been reduced somewhat above 30 km to compensate for this effect. Our predicted methane and nitrous oxide concentrations, shown in figure 2(b), are in good agreement with the limited observations that are available.

We have recently developed an aerosol particle model to complement our one-dimensional photochemical model. The aerosol physics treated in the model, and the numerical procedures required to solve the related aerosol continuity equations, are described in detail elsewhere (ref. 10). In the model, SO_2 and OCS molecules diffuse upward from the troposphere into the stratosphere; sulfur gases are also injected there by volcanoes (and aircraft). At high altitudes OCS is photolytically decomposed by ultraviolet radiation, and the products quickly react to form SO_2 (ref. 33). Sulfur dioxide is subsequently oxidized into sulfuric acid vapor via the intermediary radical HSO_3, which is assumed to have a short chemical lifetime in air. Once formed, H_2SO_4 molecules nucleate with water vapor onto

condensation nuclei which are also transported upward from the troposphere. The resulting acid solution droplets continue to grow by heteromolecular condensation of water and acid vapors, coagulate with one another, settle gravitationally, and diffuse by turbulent mixing. Droplets that rise above the aerosol layer (to about 30 km) evaporate rapidly to their bare cores, which settle again to lower altitudes. Evaporation is a source of H_2SO_4 molecules above the aerosol layer, but this does not materially affect the shape of the layer. Our model also follows the accumulation and evolution of the solid cores within the aerosol droplets.

Preliminary calculations with the aerosol model are in excellent agreement with numerous observations of the natural particulate layer. The computed peak mass mixing ratio for the layer is near 21 km, some 8 km above the tropopause, as observed. Particle number mixing ratios are close to measured values, and the droplet size distribution and composition are also correctly reproduced.

Several feedback mechanisms are built into our atmospheric model. Of course, the photochemistry and parameterized dynamics are completely interactive, which significantly influences the response of the model atmosphere to simulated perturbations. Aerosol particles can also interact with the gaseous compounds in our simulation, although we have not yet included possible radiation and surface catalysis feedback effects. The ozone profile in our model controls, to a large extent, the ultraviolet radiation fluxes reaching the stratosphere. Accordingly, we recalculate all of the photodissociation rates (and rescale the rate constants during diurnally averaged runs) whenever the integrated ozone column above 10 km, or above 30 km, changes by a specific fractional amount. This fraction is usually selected to be small relative to the expected ozone variation in order to achieve good numerical resolution without having to recalculate the photorates at each time step, which is very inefficient.

We have developed a stratospheric temperature model that utilizes the ozone ultraviolet heating rates of Lacis and Hansen (ref. 34) and the CO_2 infrared cooling rates of Dickinson (ref. 35). The air temperatures are recalculated whenever the ozone abundance changes significantly, as described above. The atmospheric scale heights and densities and the rate constants are also redetermined at these times. The temperature subroutine is presently inactive in our model since we discovered by experimentation that temperature feedback effects on ozone concentrations were only about 10 percent or less of the overall ozone variation (resulting in slightly smaller predictions of ozone reductions in polluted air). Moreover, we do not feel that parameterized treatments of heating and cooling that neglect the related effects on atmospheric dynamics are valid for the large ozone perturbations often studied with our model.

Finally, we mention another unique feedback mechanism in our model which is related to the use of families of species. Our numerical solution of the family continuity equations is largely independent of the solution for the individual species distributions. However, in order for the complete computation to be stable and to proceed to a steady state, these two distinct

solutions must converge to the same species concentrations. Hence, in our code we have a built-in detector of numerical inconsistencies.

OPERATIONAL MODES FOR MODEL CALCULATIONS

Our computer model is organized so that we only need to flag several input parameters in order to control the mode of calculation and the printing and plotting of output data. The choices for computing photodissociation rates, and the optional diurnal averaging scheme, have been discussed earlier. The basic temporal modes of operation are:

1. Steady-state runs which extend for a specified time duration.

2. Time-dependent calculations which are similar to steady-state runs except that certain parameters may have explicit time variations, and data at intermediate times are of interest.

3. Diurnal simulations where, in order to achieve rapid solution convergence, we usually use diurnally averaged steady-state species profiles as initial conditions.

In any of these temporal modes, we can add physical perturbations to the system. The most important of these are:

1. Supersonic transport exhaust: We inject SST effluents (NO, H_2O, SO_2) uniformly in hemispherical or global shells, the amount and altitude profile depending on the engine, traffic, and flight path models.

2. Space shuttles: We add HCl and NO from the shuttle launch rockets, spread hemispherically or globally, with an altitude profile characteristic of these vehicles at a rate determined by the launch schedule.

3. Fluorocarbons: Starting with a steady-state ambient atmosphere, we inject CF_2Cl_2 and $CFCl_3$ at the ground at globally averaged rates (which may remain constant or change with time, and may end abruptly). Each fluorocarbon is allowed to accumulate in the troposphere at a rate proportional to the difference between its input flux at the surface and its escape flux into the stratosphere (or into the lower model boundary at 10 km). Thus, we solve the time-dependent growth equations for the tropospheric fluorocarbon content, and we couple these solutions to the one-dimensional model through the boundary conditions at 10 km. As we have always done, we allow for the possibility of tropospheric loss mechanisms for CF_2Cl_2 and $CFCl_3$ by assigning them average tropospheric lifetimes (from 30 years to ∞).

CONCLUDING REMARKS

We have presented a complete and concise outline of our one-dimensional atmospheric computer simulation. Some of the unique aspects of our model which we have described above are:

1. A technique for obtaining rapid and accurate solutions of species continuity equations using the concept of conserved families of aeronomically related compounds.

2. An averaging scheme for simulating effects of diurnal variations on atmospheric constituent concentrations.

3. An efficient O_2 Schumann-Runge band absorption model for computing molecular photodissociation rates.

4. A detailed simulation of aerosol particle formation and evolution in the Earth's stratosphere.

As we mentioned in the Introduction, specific examples of our model predictions can be found in the literature.

Ames Research Center
National Aeronautics and Space Administration
Moffett Field, Calif. 94035, April 14, 1977

REFERENCES

1. Turco, R. P.; and Whitten, R. C.: A Comparison of Several Computational Techniques for Solving Some Common Aeronomic Problems. J. Geophys. Res., vol. 79, no. 22, 1974, pp. 3179-3185.

2. Turco, R. P.: Photodissociation Rates in the Atmosphere Below 100 km. Geophys. Surveys, vol. 2, no. 2, 1975, pp. 153-192.

3. Turco, R. P.; and Whitten, R. C.: A Note on the Diurnal Averaging of Aeronomical Models. J. Atmos. Terr. Phys., 1977. (To be published.)

4. Whitten, R. C.; Sims, J. S.; and Turco, R. P.: A Model of Carbon Compounds in the Stratosphere and Mesosphere. J. Geophys. Res., vol. 78, no. 24, 1973, pp. 5362-5374.

5. Whitten, R. C.; and Turco, R. P.: Perturbations of the Stratosphere and Mesosphere by Aerospace Vehicles. AIAA J., vol. 12, no. 8, 1974, pp. 1110-1117.

6. Whitten, R. C.; and Turco, R. P.: Diurnal Variations of HO_x and NO_x in the Stratosphere. J. Geophys. Res., vol. 79, no. 9, 1974, pp. 1302-1304.

7. Whitten, R. C.; Borucki, W. J.; Poppoff, I. G.; and Turco, R. P.: Preliminary Assessment of the Potential Impact of Solid-Fueled Rocket Engines in the Stratosphere. J. Atmos. Sci., vol. 32, no. 3, 1975, pp. 613-619.

8. Whitten, R. C.; Borucki, W. J.; and Turco, R. P.: Possible Ozone Depletions Following Nuclear Explosions. Nature, vol. 257, no. 5521, 1975, pp. 38-39.

9. Turco, R. P.; and Whitten, R. C.: Chlorofluoromethanes in the Stratosphere and Some Possible Consequences for Ozone. Atmos. Environ., vol. 9, no. 12, 1975, pp. 1045-1061.

10. Turco, R. P.; Hamill, P.; Toon, O. B.; and Whitten, R. C.: A Model of the Stratospheric Aerosol. Atmospheric Aerosols: Their Optical Properties and Effects. A Topical Meeting on Atmospheric Aerosols, Williamsburgh, Va., Dec. 1976. NASA CP-2004, 1976.

11. Colegrove, F. D.; Johnson, F. S.; and Hanson, W. B.: Atmospheric Composition in the Lower Thermosphere. J. Geophys. Res., vol. 71, no. 9, 1966, pp. 2227-2236.

12. Ames, William F.: Numerical Methods for Partial Differential Equations. Barnes and Nobel, New York, 1969.

13. Burnett, Clyde R.: Terrestrial OH Abundance Measurement by Spectroscopic Observation of Resonance Absorption of Sunlight. Geophys. Res. Lett., vol. 3, no. 6, 1976, pp. 319-322.

14. Anderson, J. G.: The Absolute Concentration of OH($X\ ^2\Pi$) in the Earth's Stratosphere. Geophys. Res. Lett., vol. 3, no. 3, 1976, pp. 165-168.

15. Ackerman, M.: Ultraviolet Solar Radiation Related to Mesospheric Processes. Mesospheric Models and Related Experiments, G. Fiocco, ed., D. Reidel, Dordrecht, Holland, 1971, pp. 149-159.

16. Donnelly, R. F.; and Pope, J. H.: The 1-3000 Å Solar Flux for a Moderate Level of Solar Activity for Use in Modeling the Ionosphere and Upper Atmosphere. NOAA Tech. Rep. ERL 276-SEL-25, 1973.

17. Heroux, L.; and Swirbalus, R. A.: Full-Disk Solar Fluxes Between 1230 and 1940 Å. J. Geophys Res., vol. 81, no. 4, 1976, pp. 436-440.

18. Luther, Frederick M.; and Gelinas, Robert J.: Effect of Molecular Multiple Scattering and Surface Albedo on Atmospheric Photodissociation Rates. J. Geophys. Res., vol. 81, no. 6, 1976, pp. 1125-1132.

19. Swider, William, Jr.: The Determination of the Optical Depth at Large Solar Zenith Distances. Planet. Space Sci., vol. 12, no. 8, 1964, pp. 761-782.

20. Swider, William, Jr.; and Gardner, M. E.: On the Accuracy of Certain Approximations for the Chapman Function. Air Force Cambridge Research Labs. Environmental Res. Paper 272, Aug. 1967.

21. Hudson, Robert D.; and Mahle, Stephen H.: Photodissociation Rates of Molecular Oxygen in the Mesosphere and Lower Thermosphere. J. Geophys. Res., vol. 77, no. 16, 1972, pp. 2902-2914.

22. Blake, A. J.; Carver, J. H.; and Haddad, G. N.: Photoabsorption Cross Sections of Molecular Oxygen Between 1250 Å and 2350 Å. J. Quant. Spectrosc. Radiat. Trans., vol. 6, no. 4, 1966, pp. 451-459.

23. Brinkmann, R. T.: Dissociation of Water Vapor and Evolution of Oxygen in the Terrestrial Atmosphere. J. Geophys. Res., vol. 74, no. 23, 1969, pp. 5355-5368.

24. Whitten, R. C.; Borucki, W. J.; and Turco, R. P.: One-Dimensional Model Studies of Ozone Depletion. Proc. Third CIAP Conf., U.S. Dept. of Transportation Rep. DOT-TSC-OST-74-15, 1974, pp. 342-358.

25. Kuis, Susan; Simonaitis, R.; and Heicklen, Julian: Temperature Dependence of the Photolysis of Ozone at 3130 Å. J. Geophys. Res., vol. 80, no. 10, 1975, pp. 1328-1331.

26. Kajimoto, O.; and Cvetanovic, R. J.: Temperature Dependence of $O(^1D_2)$ Production in the Photolysis of Ozone at 313 nm. Chem. Phys. Lett., vol. 37, no. 3, 1976, pp. 533-536.

27. Johnston, H. S.; and Selwyn, G. S.: New Cross Sections for the Absorption of Near Ultraviolet Radiation by Nitrous Oxide (N_2O). Geophys. Res. Lett., vol. 2, no. 12, 1975, pp. 549-551.

28. Inn, Edward C. Y.: Absorption Coefficients for HCl in the Region 1400-2200 Å. J. Atmos. Sci., vol. 32, no. 12, 1975, pp. 2375-2377.

29. Rowland, F. S.; Spencer, John E.; and Molina, Mario J.: Stratospheric Formation and Photolysis of Chlorine Nitrate. J. Phys. Chem., vol. 80, no. 24, 1976, pp. 2711-2713.

30. Cogley, Allen C.; and Borucki, William J.: Exponential Approximation for Daily Average Solar Heating or Photolysis. J. Atmos. Sci., vol. 33, no. 7, 1976, pp. 1347-1356.

31. Wofsy, Steven C.; and McElroy, Michael B.: On Vertical Mixing in the Upper Stratosphere and Lower Mesosphere. J. Geophys. Res., vol. 78, no. 15, 1973, pp. 2619-2624.

32. Johnston, Harold S.; Kattenhorn, David; and Whitten, Gary: Use of Excess Carbon 14 Data to Calibrate Models of Stratospheric Ozone Depletion by Supersonic Transports. J. Geophys. Res., vol. 81, no. 3, 1976, pp. 368-380.

33. Crutzen, Paul J.: The Possible Importance of CSO for the Sulphate Layer of the Stratosphere. Geophys. Res. Lett., vol. 3, no. 2, 1976, pp. 73-76.

34. Lacis, Andrew A.; and Hansen, James E.: A Parameterization for the Absorption of Solar Radiation in the Earth's Atmosphere. J. Atmos. Sci., vol. 31, no. 1, 1974, pp. 118-133.

35. Dickinson, Robert E.: Method of Parameterization for Infrared Cooling between Altitudes of 30 and 70 Kilometers. J. Geophys. Res., vol. 78, no. 21, 1973, pp. 4451-4457.

36. Ehhalt, D. H.; Heidt, L. E.; and Martell, E. A.: The Concentration of Atmospheric Methane between 44 and 62 km Altitude. J. Geophys. Res., vol. 77, no. 12, 1972, pp. 2193-2196.

37. Ehhalt, D. H.; and Heidt, L. E.: Vertical Profiles of CH_4 in the Troposphere and Stratosphere. J. Geophys. Res., vol. 78, no. 24, 1973, pp. 5265-5273.

38. Ehhalt, D. H.; Heidt, L. E.: Lueb, R. H.; and Roper, N.: Vertical Profiles of CH_4, H_2, CO, N_2O, and CO_2 in the Stratosphere. Proc. Third CIAP Conf., Rep. DOT-TSC-OST-74-15, U.S. Dept. of Transportation, 1974, pp. 153-160.

39. Ehhalt, D. H.: Sampling of Stratospheric Trace Constituents. Can. J. Chem., vol. 52, no. 8, 1974, pp. 1510-1518.

1. Report No.	2. Government Accession No.	3. Recipient's Catalog No.
NASA TP-1002		

4. Title and Subtitle	5. Report Date
THE NASA AMES RESEARCH CENTER ONE- AND TWO-DIMENSIONAL STRATOSPHERIC MODELS. PART I: THE ONE-DIMENSIONAL MODEL	September 1977
	6. Performing Organization Code

7. Author(s)	8. Performing Organization Report No.
R. P. Turco and R. C. Whitten	A-6983
	10. Work Unit No. 197-30-02

9. Performing Organization Name and Address	11. Contract or Grant No.
R and D Associates, Marina Del Rey, Calif. 90291 and Ames Research Center, Moffett Field, Calif. 94035	

12. Sponsoring Agency Name and Address	13. Type of Report and Period Covered
National Aeronautics and Space Administration, Washington, D.C. 20546	Technical Paper
	14. Sponsoring Agency Code

15. Supplementary Notes

16. Abstract

A one-dimensional model of stratospheric trace constituents, developed in a joint effort by scientists at Ames Research Center and at R and D Associates, is described in detail. Specifically, the numerical solution of the species continuity equations, including a technique for treating the "stiff" differential equations representing the chemical kinetic terms, and an appropriate method for simulating the diurnal variation of the species concentrations, are discussed. A specialized treatment of atmospheric photodissociation rates is outlined in the text. The choice of a vertical eddy diffusivity profile and its success in predicting the vertical tracer distributions (carbon 14, methane, and nitrous oxide) are also discussed.

17. Key Words (Suggested by Author(s))	18. Distribution Statement
Stratosphere Atmosphere model Atmospheric photochemistry	Unlimited STAR Category - 47

19. Security Classif. (of this report)	20. Security Classif. (of this page)	21. No. of Pages	22. Price*
Unclassified	Unclassified	30	$3.75

*For sale by the National Technical Information Service, Springfield, Virginia 22161

NASA-Langley, 1977

581 001 C1 U E 770819 S00903DS
DEPT OF THE AIR FORCE
AF WEAPONS LABORATORY
ATTN: TECHNICAL LIBRARY (SUL)
KIRTLAND AFB NM 87117